Chinese Chemical Letters 34 (2023) 107137

Contents lists available at ScienceDirect

Chinese Chemical Letters

journal homepage: www.elsevier.com/locate/cclet

Metal-organic frameworks derived low-crystalline $NiCo_2S_4/Co_3S_4$ nanocages with dual heterogeneous interfaces for high-performance supercapacitors

Zixin Jia[a], Youning Wang[a], Jiaqi Chen[a,b], Zhijie Cao[c], Shugang Pan[a,d], Yan Zhou[a], Jingwen Sun[a], Junwu Zhu[a], Xin Wang[a], Yongsheng Fu[a,*]

[a] Key Laboratory for Soft Chemistry and Functional Materials of Ministry of Education, Nanjing University of Science and Technology, Nanjing 210094, China
[b] Jiangsu Key Laboratory for Chemistry of Low-Dimensional Materials, Huaiyin Normal University, Huaiyin 223300, China
[c] Ningxia University, Yinchuan 750021, China
[d] Changzhou Institute of Technology, Changzhou 213032, China

ARTICLE INFO

Article history:
Received 16 November 2021
Revised 31 December 2021
Accepted 11 January 2022
Available online 16 January 2022

Keywords:
Metal-organic frameworks
Nickel cobalt heterogeneous sulfides
Low-crystalline nanostructure
High-performance supercapacitors
High energy density

ABSTRACT

Nickel cobalt bimetallic heterogeneous sulfides are attractive battery-type materials for electrochemical energy storage. However, the precise synthesis of electrode materials that integrate highly efficient ions/electrons diffusion with abundant charge transfer channels has always been challenging. Herein, an effective and concise controllable hydrothermal approach is reported for tuning the crystalline and integrated structures of MOF-derived bimetallic sulfides to accelerate the charge transfer kinetics, and thus enabling rich Faradaic redox reaction. The as-obtained low-crystalline heterogeneous $NiCo_2S_4/Co_3S_4$ nanocages exhibit a high specific capacity (1023 C/g at 1 A/g), remarkable rate performance (560 C/g at 10 A/g), and outstanding cycling stability (89.6% retention after 5000 cycles). Furthermore, hybrid supercapacitors fabricated with $NiCo_2S_4/Co_3S_4$ and nitrogen-doped reduced graphene oxide display an outstanding energy density of 40.8 Wh/kg at a power density of 806.3 W/kg, with an excellent capacity retention of 88.3% after 10000 charge-discharge cycles.

In the past decades, the demand for developing durable and sustainable energy storage and conversion technologies has continued to increase due to the energy crisis and extensive environmental problems caused by the rapidly continuous combustion of fossil fuels [1,2]. In this regard, high-efficiency electrochemical energy storage devices as an essential component in the development of advanced energy systems have received significant research attention [3–5]. Among them, supercapacitors (SCs), also called ultracapacitors or electrochemical capacitors, show desirable properties of fast charging/discharging, high power density and excellent cycling stability over other conventional energy storage devices [6,7]. Especially, compared to commercially available supercapacitors based on carbonaceous electrode materials, hybrid supercapacitors (HSCs) consisting of a battery-type electrode (for high specific energy) and a capacitive electrode (for great specific power and long lifespan) could obtain even higher energy performances because of the integration of these two electrodes [8,9]. However, the practical applications of hybrid supercapacitors are still hampered by the relatively moderate properties of the electrode materials [10]. To address this issue, exploring of advanced electroactive electrode materials is very exigent for developing new-type hybrid supercapacitors with extraordinary merits of high energy and power density.

Metal-organic frameworks (MOFs), a series of porous compounds interconnected by periodic inorganic-organic linker, have attracted much research attention in emerging electrochemical energy storage applications due to their high crystallinity, tunable sub-structure and various multifunctionalities [11–17]. As a class of bifunctional materials with metal ions precursors and sacrificial templates, MOFs and their derived composites such as carbon-based nanocomposites and metal oxides/sulfides/phosphides are extensively exploited as electrode materials for supercapacitors [18–25]. Among of them, transition metal sulfides have shown overwhelming advantages on account of their enhanced conductivity, abundant electrochemically active sites, and high theoretical specific capacities compared with the oxide counterpart [26,27]. Moreover, the construction of bimetallic sulfides heterostructures, which can create abundant heterointerfaces between separate components and induce substantial interfacial electron transfer

* Corresponding author.
E-mail address: fuyongsheng@njust.edu.cn (Y. Fu).

https://doi.org/10.1016/j.cclet.2022.01.030
1001-8417/

to promote ion and electron transport properties, have displayed novel structural features and considerable exposed active sites [28,29]. Plenty of efforts have been devoted to designing hierarchical heterogeneous structures, such as $Cu(OH)_2/Cu_7S_4$ hybrid nanowires [30], NiS_2/MoS_2 composites [31], double-layered yolk-shell $NiCo_2S_4$-Ni_9S_8-C microspheres [32]. However, the preparation of these composites includes lengthy steps, which makes the synthesis time-consuming and thus limits their practical applications [33]. Thus, it is highly desirable to optimize the preparation procedures to mitigate these limitations.

In the process of exploring various high-performance electrode materials, tremendous efforts have been devoted to designing transition metal sulfides with tunable crystallinity and electronic structure to activate redox-active metal sulfides spices and boost highly-reversible and fast reactions [34,35]. With the merit of facilitating the charge transfer during redox reactions and maximizing the use of edge sites, well-crystalline nanocomposites possess superior electrical conductivities and enhanced electrode kinetics [36–38]. For instance, Ren *et al.* reported $Co_{1-x}S/CoFe_2O_4$@rGO nanoflowers through controlling the calcined sulfurization temperature to obtain a well-crystalline hierarchical-pore structure with a high specific capacity of 2202 F/g and superior cycling stability [39]. Liu *et al.* designed a simple strategy to grow Co_9S_8-$NiCo_2S_4$ core-shell nanoneedle films with high crystallinity on carbon cloth and the metal sulfide electrodes exhibit superior electrochemical ability [40]. However, these as-prepared well crystallized metal sulfides structures are incapable of expanding or contracting during large-current charge/discharge, thus limiting the ions/electrons permeation and diffusion [41]. By comparison, poor-crystalline or amorphous phase materials afford high structural disorder, abundant active sites, and effective charge transfer channels [42]. Nevertheless, the introduction of amorphous phase also generates relatively large resistance inside electrodes during charge transfer and eventually lead to inferior electrochemical performance [43]. Therefore, it has become a critical step to rationalize the crystalline structure for exploring low-crystalline mental sulfides that can make sufficient active sites, boost charge transfer and ion diffusion.

Given the adaptability of self-templated MOFs in the fabrication of heterogeneous structures and the advantages of low-crystalline mental sulfides, we present the synthesis of MOF-derived low-crystalline heterogeneous $NiCo_2S_4/Co_3S_4$ nanocages (NCs) that possesses synergetic electrochemical properties within an integral framework. Using sacrificial ZIF-67 template as a precursor, *in situ* chemical transformation of Ni-Co layered double hydroxide (NiCo-LDH) into low-crystalline heterogeneous $NiCo_2S_4/Co_3S_4$ hollow polyhedron was carried out through a controllable hydrothermal methodology. The resulting composite electrode exhibits a superior specific capacity of 1023 C/g at 1 A/g and outstanding cycling stability (89.6% over 5000 cycles at 10 A/g). Furthermore, a hybrid supercapacitor (HSC) assembled with $NiCo_2S_4/Co_3S_4$ NCs and nitrogen-doped reduced graphene oxide (referred as N-rGO) achieves synchronous high energy density of 40.8 Wh/kg and power density up to 8595.6 W/kg, as well as excellent cyclic stability.

The fabrication process of $NiCo_2S_4/Co_3S_4$ NCs is schematically demonstrated in Fig. 1a. Through a simple room-temperature solution reaction approach, well-defined ZIF-67 nanocrystals with rhombic dodecahedron shape were first synthesized by the co-precipitation method of cobalt ions as the metallic node and 2-methylimidazole as the organic linker. The field-emission scanning electron microscopy (FESEM) images show that the ZIF-67 nanocrystals exhibited solid polygonal structures with smooth surface and particle size ranged from 1 μm to 2 μm (Figs. 1b and e, Fig. S1a in Supporting information). X-ray diffraction (XRD) pattern (Fig. S1b in Supporting information) matches well with simulated and previous reports [44], clearly indicating the successful synthesis of ZIF-67 nanocrystals. Subsequently, the as-prepared ZIF-67 nanocrystals were acted as sacrificial templates to prepare NiCo-LDH by etching process under the effect of $Ni(NO_3)_2{\cdot}6H_2O$. By releasing hydroxyl and nickel ions from the hydrolysis of nickel nitrate in ethanol, protons generated from the hydrolysis of Ni^{2+} gradually etched ZIF-67 crystals from the surface to skeleton, and eventually the released Co^{2+}/Co^{3+} coprecipitated with Ni^{2+} to form hollow NiCo-LDH nanocages. The derived NiCo-LDH hollow polyhedral particles composed of interconnected loosely packed LDH nanoflakes maintain the rhombic dodecahedral structure with rough surfaces (Figs. 1c and f). Finally, through solvothermal reaction, NiCo-LDH was converted to heterogeneous $NiCo_2S_4/Co_3S_4$ NCs with TAA as the sulfur source, which exhibit the polyhedron morphology and relatively slight contraction in structure, hence retaining the original ZIF-67 sacrificial template structure (Figs. 1d and g). During this etching process, the uniformly distributed nanosheets on the shell of the NiCo-LDH become disorder and thicker, and the Ni-ions and Co-ions within NiCo-LDH framework were converted to nickel and cobalt sulfides (NCS), generating the final $NiCo_2S_4/Co_3S_4$ composite.

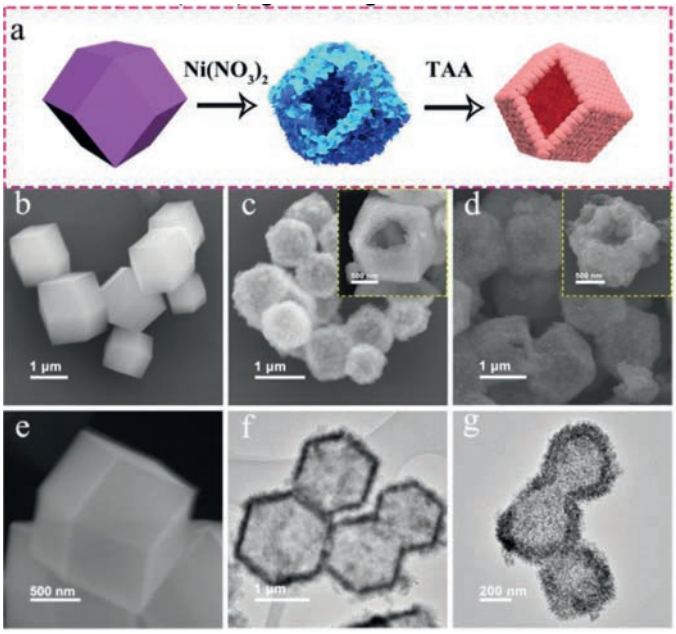

Fig. 1. (a) Schematic illustration of the synthetic procedure of $NiCo_2S_4/Co_3S_4$ NCs. (b, e) FESEM images of ZIF-67 crystals. (c) FESEM and (f) TEM images of NiCo-LDH. (d) FESEM and (g) TEM images of $NiCo_2S_4/Co_3S_4$. The inset in (c) and (d) are the single SEM images of NiCo-LDH and $NiCo_2S_4/Co_3S_4$.

The microstructure features and chemical composition of NiCo-LDH and $NiCo_2S_4/Co_3S_4$ were meticulously characterized using transmission electron microscopy (TEM) and high-resolution TEM (HRTEM). Figs. 2a-c and Fig. S2a (Supporting information) are the typical TEM images of NiCo-LDH composite obtained by the solvothermal reaction of ZIF-67 nanocrystals with $Ni(NO_3)_2{\cdot}6H_2O$ at 120 °C for 4 h. It can be observed that the initial vice-like outer structure of the ZIF-67 framework was totally etched away and decorated by interconnected ultrathin and wrinkled nanosheets. Meanwhile, the well-defined hollow interior is perspicuously demonstrated. As illustrated in Fig. S2a, well-defined diffraction rings in the selected electron diffraction (SAED) pattern suggest the good crystallinity properties of NiCo-LDH, which can be indexed to the (012) and (110) planes. Furthermore, the HRTEM image (Fig. S2b in Supporting information) exhibits the regular lattice fringes with inter planar distance of 0.26 nm, corresponding to the (012) plane of NiCo-LDH. As characterized by the elemental

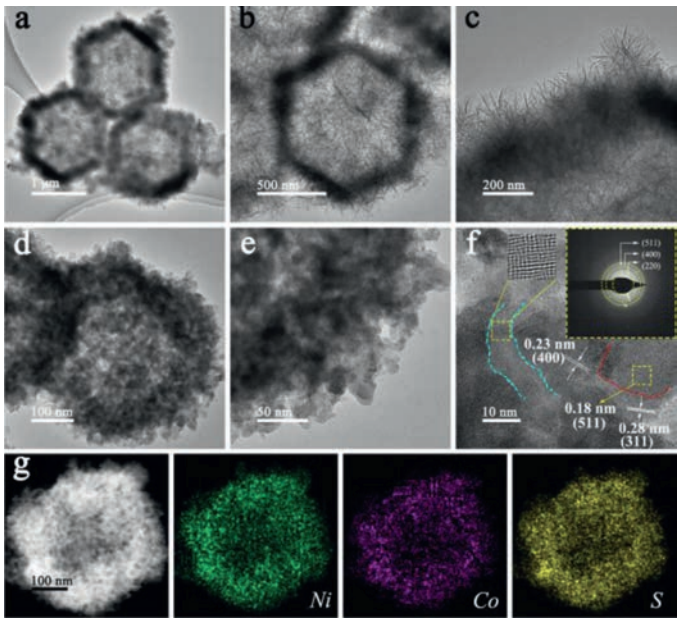

Fig. 2. TEM and high-resolution TEM images of (a-c) NiCo-LDH and (d-f) $NiCo_2S_4/Co_3S_4$. The inset in (f): the corresponding SAED pattern. (g) HAADF image and the corresponding elemental mapping of $NiCo_2S_4/Co_3S_4$ for Ni, Co and S.

mapping images, the Ni, Co and O elements are homogeneously distributed throughout the whole NiCo-LDH frame. The large numbers of small-sized nanosheets in-situ formed on the surface can not only be favorable for making more redox-active sites but also offer beneficial conditions for the next step of fabricating the nickel and cobalt sulfides.

After the sulfuration process of NiCo-LDH with TAA at 120 °C for 4 h, TEM with higher magnification images (Figs. 2d and e) show that the morphology of nanocages is well maintained, and the original LDH nanosheets on the surface become thicker and partially granulating to nanoparticles (NPs). The highly uniform and discrete $NiCo_2S_4/Co_3S_4$ NPs are embedded in the wall of the original dodecahedron framework. Further investigations show clear lattice fringes with interplanar distance of 2.3 Å and 2.8 Å measured from the HRTEM image can be ascribed to the (400) and (311) crystals planes of the $NiCo_2S_4$, and an interplanar spacing value of 1.8 Å can be indexed to crystals planes of Co_3S_4 (511). The different regions separated by the red dotted line reveal the hybrid structure of $NiCo_2S_4/Co_3S_4$ NPs. Moreover, the diffraction rings of selected-area electron diffraction pattern (Fig. 2f inset) also reveal the coexistence and polycrystalline nature of $NiCo_2S_4$ and Co_3S_4 in $NiCo_2S_4/Co_3S_4$ NCs.

However, the internal regions marked by yellow squares, obtained by inverse fast Fourier transform (FFT), indicate the existence of lattice dislocation and blurred lattice borders, and these regions are evenly dispersed in the simples. Also, three different types of crystallinities are displayed in the regions marked by the blue dotted line, indicates the abundant interfaces of amorphous, low-crystalline, and well crystallized structures. The numerous amorphous regions, as well as messy and distorted lattice fringes surrounded by distinct crystalline domain imply that the as-obtained $NiCo_2S_4/Co_3S_4$ NCs have a comparatively poor crystallinity. Consequently, the abundant grain boundaries and heterointerfaces created by these highly discrete $NiCo_2S_4/Co_3S_4$ NPs can induce strong interfacial electron transfer properties, promote immersion of the electrolyte ions, and provide more interfacial active sites for the redox reaction [45]. High-angle annular dark-field scanning TEM (HAADF-STEM) image of one single nanocage confirms its rough and porous feature, and the corresponding energy-dispersive X-ray spectroscopy (EDS) profiles show a relatively uniform distribution of Ni, Co and S throughout the whole $NiCo_2S_4/Co_3S_4$ NC (Fig. 2g). Hence, a low-crystalline heterogeneous electroactive material containing $NiCo_2S_4/Co_3S_4$ NPs embedded in a hollow nanostructure was formed in-situ by this simple two-step process.

The crystal structure and coexistence of phases at each evolution steps were carried out by X-ray diffraction technique (XRD), and the results are shown in Fig. 3a. Diffraction patterns of NiCo-LDH are indexed to (003), (006), (012) and (110) plane reflections of the hydrotalcite-like LDH phase with characteristic diffraction peaks of 11.8°, 24.5°, 33.5° and 59.7°. All ZIF-67 diffraction peaks are missing, declaring the complete transformation of ZIF-67 crystal into NiCo-LDH, consistent with the SEM observation (Fig. 1) for the formation of hollow nanocages and the FTIR analysis (Fig. 3b). To investigate the effect of sulfuration on the phase composition and morphology, the NiCo-LDH precursor were also processed with TAA for 2 h, 6 h and 9 h at 120 °C. For the sample of NCS-2, the diffraction peaks are similar to the NiCo-LDH. The morphology of the NCS-2 is almost the same as NiCo-LDH with less densely packed nanosheets covered shell (Figs. S3a and b in Supporting information). For NCS-4 nanohybrids, the weaker diffraction peaks observed at 31.4° and 38.1° are well-aligned with $NiCo_2S_4$ structure (JCPDS card No. 43-1477), while the other two well-defined peaks observed at 50.2° and 54.9° can be indexed to (511) and (440) plane reflections of the Co_3S_4 structure (JCPDS card No. 11-0121) due to relatively complete sulfuration process. The above-mentioned XRD analysis of simple NCS-4 are in good agreement with HRTEM images, demonstrating the successful synthesis of unique heterogeneous $NiCo_2S_4/Co_3S_4$ NCs. With the solvothermal reaction time extending, the surface of NCS-6 and NCS-9 accompanied by innumerous glomerate nanoparticles became extremely rougher, and the hollow porous structure slightly collapsed due to sufficient anions exchange reaction (Figs. S3c-f in Supporting information). Moreover, the diffraction peaks of XRD for both NCS-6 and NCS-9 are well aligned with NiS_2 structure (JCPDS card No. 03-0734) with an apparent well-crystalline structure. Moreover, BET surface area analysis were performed on the prepared NiCo-LDH and $NiCo_2S_4/Co_3S_4$ samples.

The corresponding N_2 adsorption/desorption isotherms are shown in Fig. S4 (Supporting information). There are typical type-IV isotherms, confirming the mesoporous characteristics of the samples (Figs. S4a and c). Although the calculated specific surface area of NiCo-LDH (140.28 m^2/g) was higher than $NiCo_2S_4/Co_3S_4$ (15.61 m^2/g), the $NiCo_2S_4/Co_3S_4$ exhibits pores with larger diameters arising from the formation of the self-assembling of nickel and cobalt sulfide nanoparticles (Figs. S4b and d), which can act as ion-buffering reservoirs to minimize the diffusion distance from the bulk electrolyte to the surface of the active material, eventually improving the electrochemical performance [46].

To characterize the elemental composition and electronic states of the $NiCo_2S_4/Co_3S_4$ NCs, X-ray photoelectron spectroscopy (XPS) characterizations are conducted. The survey spectra (Fig. 3c) demonstrate the existence of Ni, Co O and S elements in the as-synthesized $NiCo_2S_4/Co_3S_4$ NCs, which is consistent with the EDX analysis (Fig. 2g). In the case of the Ni 2p spectrum of NiCo-LDH (Fig. 3d), a significant spin-orbit bimodal and two vibrating satellites (denoted as "Sat.") located at 855.6 eV and 873.2 eV can be attributed to the Ni $2p_{3/2}$ and Ni $2p_{1/2}$ signals of Ni^{2+}, respectively [37,47,48]. The Co 2p spectrum is exhibited in Fig. 3e, two major peaks centered at 781.0 eV and 796.6 eV correspond to Co $2p_{3/2}$ and Co $2p_{1/2}$. Furthermore, peaks observed at 780.9 eV and 796.3 eV are attributed to Co^{3+}, and peaks located at 783.0 and 797.8 eV correspond to Co^{2+}, suggestive of the existence of Co^{3+}

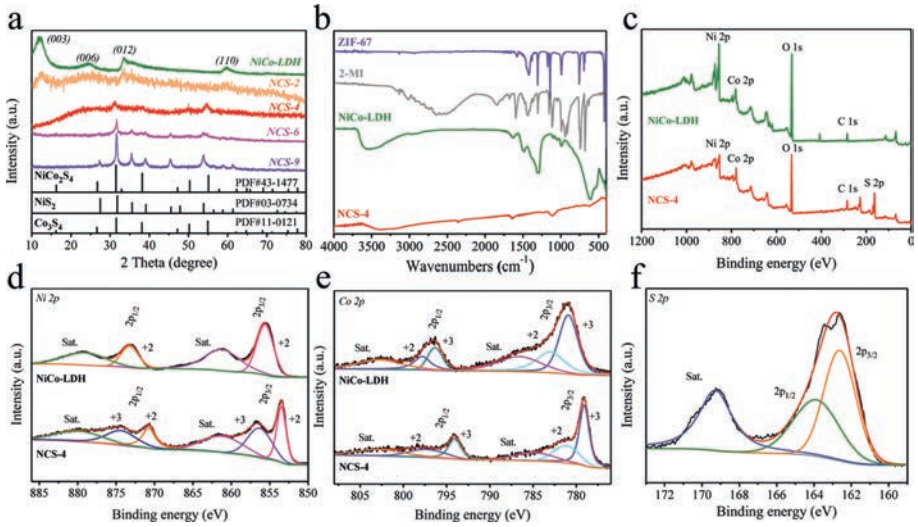

Fig. 3. (a) XRD patterns of NiCo-LDH, NCS-2, NCS-4, NCS-6 and NCS-9. (b) FTIR spectra of ZIF-67, 2-methylimidazole (2-MI), NiCo-LDH and NCS-4. (c) XPS full survey spectra of NiCo-LDH and NCS-4. (d) Ni 2p, (e) Co 2p high resolution XPS spectra of NiCo-LDH and NCS-4. (f) S 2p high resolution XPS spectra of NCS-4.

and Co^{2+}. In the case of the Ni 2p spectrum of $NiCo_2S_4/Co_3S_4$ (NCS-4) (Fig. 3d), the fitted peaks at 853.4 eV and 870.7 eV correspond to the $2p_{3/2}$ and $2p_{1/2}$ of Ni^{2+}, and the other two peaks at 856.4 eV and 874.4 eV could be ascribed to the $2p_{3/2}$ and $2p_{1/2}$ of Ni^{3+} [49]. The peaks (Fig. 3e) for Co $2p_{3/2}$ and Co $2p_{1/2}$ located at 779.1 eV and 794.0 eV indicate the existence of both Co^{3+} and Co^{2+}. For the S 2p spectrum as shown in Fig. 3f, two main peaks at 162.6 eV and 163.9 eV should be attributed to S $2p_{3/2}$ and S $2p_{1/2}$, where the peak at 162.6 eV is representative of metal-sulfur bonds while the peak at 163.9 eV should be ascribed to sulfur ions at low coordination ordinarily related to sulfur vacancies. The above discussed results are consistent with the XRD spectra and confirm the successful preparation of $NiCo_2S_4/Co_3S_4$ NCs.

A series of electrochemical measurements, cyclic voltammetry (CV), galvanostatic charge/discharge (GCD) and electrochemical impedance spectroscopy (EIS) were performed to evaluate the supercapacitor performance by coating samples on nickel foam as the working electrode in a three-electrode configuration. To further investigate the role of nickel and cobalt sulfides components influenced by different sulfurization time, the typical CV curves of NiCo-LDH, NCS-2, NCS-4, NCS-6, NCS-9 electrodes, and Ni foam were collected at a scan rate of 5 mV/s with a voltage window from 0 to 0.6 V (*vs.* Hg/HgO) in Fig. 4a. Obviously, the CV enclosed curve area of Ni foam is nearly insignificant compared to that of other electrodes, suggesting Ni foam just serves as the current collector and has almost no capacity contribution. The CV curves from other electrodes are different from the typical electric double-layer capacitors (EDLC) curves, and a pair of noticeable redox peaks can be observed, demonstrating the battery-type Faradaic behavior of the as-synthesized electrode materials [50]. Remarkably, the area under the CV curve of NCS-4 is larger than that of other samples together with a higher current response, indicating the hybrid $NiCo_2S_4/Co_3S_4$ electrode has a higher capacity performance. Meanwhile, via the comparative analysis of the GCD profiles (Fig. 4b and Fig. S5 in Supporting information), the charge storage and transport performance of the synthesized $NiCo_2S_4/Co_3S_4$ NCs is obviously superior and highly efficient to that of NiCo-LDH, NCS-2, NCS-6 and NCS-9 due to the longest discharging time, consistent with the CV results. The electrochemical reaction mechanism between $NiCo_2S_4/Co_3S_4$ and OH^- in the electrolyte are proposed as follows [32,51]:

$$NiCo_2S_4 + 2OH^- \leftrightarrow NiS_{4-2x}OH + 2CoS_xOH + 2e^- \quad (1)$$

$$CoS_xOH + OH^- \leftrightarrow CoS_xO + H_2O + e^- \quad (2)$$

$$Co_3S_4 + OH^- \leftrightarrow Co_3S_4OH^- + e^- \quad (3)$$

$$Co_3S_4OH^- + OH^- \leftrightarrow Co_3S_4O + H_2O + e^- \quad (4)$$

Fig. 4c depicts the typical CV curves of $NiCo_2S_4/Co_3S_4$ with distinct symmetric anodic and cathodic peaks at diverse scan rates from 2 mV/s to 15 mV/s. With the increase of scan rate, the area of the CV curve and the response current increase gradually, indicating highly efficient process of charge transfer kinetics. An obvious shape change is observed, which is correlated with the internal increased polarization. The gravimetric capacity at various current densities of the electrode is shown in Fig. 4d. The symmetric GCD curves reveal a reversible charge-discharge behavior and an occurrence of a potential plateaus, indicating a high level of electrochemical reversibility and Coulombic efficiency. Based on the GCD data, a high mass capacity of 1023 C/g for $NiCo_2S_4/Co_3S_4$ electrode is calculated at a current density of 1 A/g, superior to that of the electrodes reported based on metal sulfides (Table S1 in Supporting information). Even at a high current density of 10 A/g, the $NiCo_2S_4/Co_3S_4$ electrode material still achieves a specific capacity of 560 C/g, indicating an excellent rate capability. Besides, the specific capacity and corresponding rate performance of other electrode materials are also calculated in Fig. 4f. Notably, the $NiCo_2S_4/Co_3S_4$ electrode delivers improved charge storage, with a maximum specific capacity higher than those of NiCo-LDH, NCS-2, NCS-6 and NCS-9 at various current densities.

To explore the energy charge storage mechanism of the as-obtained $NiCo_2S_4/Co_3S_4$ electrode, the current contributions from diffusion-controlled and surface-controlled processes were analyzed. Based on the CV curves taken at different scan rates, the current density (I, A) abides by the power-low rule with the sweep rate (v, mV/s) for a constant voltage [39].

$$i = av^b \quad (5)$$

$$\log(i) = \log(a) + b\log(v) \quad (6)$$

where a and b are computational constants, and b is closely related to the different electrochemical processes. Surface-limited processes such as capacitance exhibit a current that is directly proportional to the sweep rate ($b = 1$). In contrast, diffusion-controlled processes (semi-infinite linear diffusion) exhibit a current response that is proportional to the square root of sweep rate ($b = 0.5$).

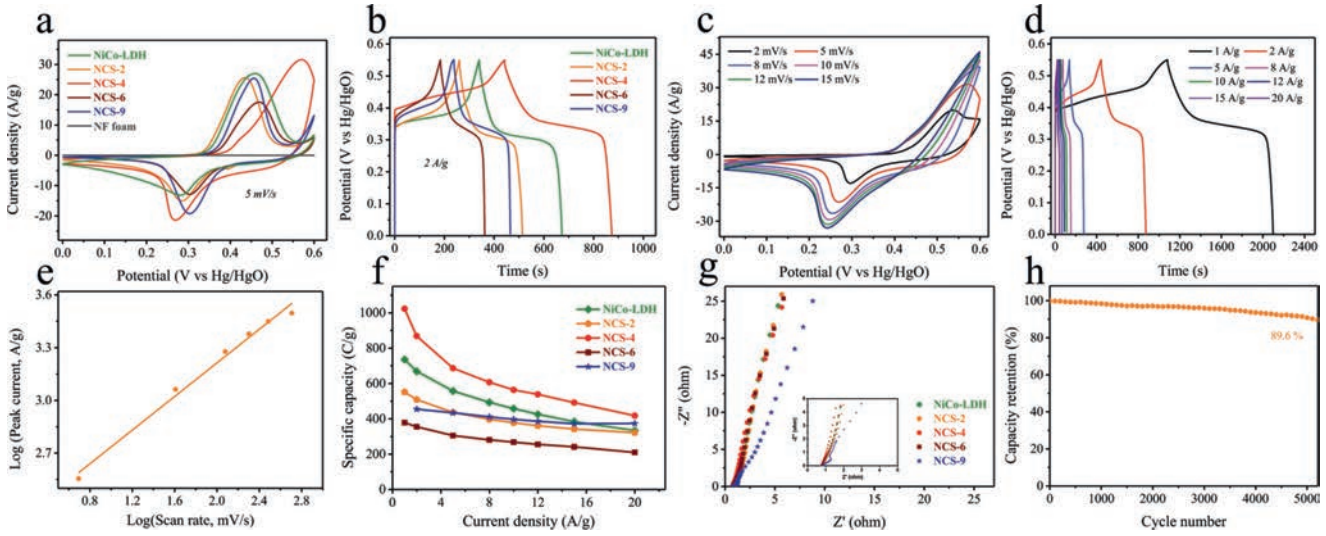

Fig. 4. (a) Comparison of the CV curves of NiCo-LDH, NCS-2, NCS-4, NCS-6, NCS-9 and Ni foam at a scan rate of 5 mV/s. (b) Comparison of the GCD curves of NiCo-LDH, NCS-2, NCS-4, NCS-6 and NCS-9 at a current density of 2 A/g. (c) CV curves of $NiCo_2S_4/Co_3S_4$ NCs at various sweep rates ranging from 0–0.6 V. (d) GCD curves of $NiCo_2S_4/Co_3S_4$ NCs at various current densities. (e) Linear relationship between logarithm of cathode peak current and logarithm of scan rates for $NiCo_2S_4/Co_3S_4$ NCs. (f) Trends of specific capacity values with current density for NiCo-LDH, NCS-2, NCS-4, NCS-6 and NCS-9 electrodes. (g) Nyquist plots of the NiCo-LDH, NCS-2, NCS-4, NCS-6 and NCS-9 electrodes, respectively. (h) Cycling performance of $NiCo_2S_4/Co_3S_4$ NCs as a function of the cycle number at a current density of 10 A/g.

The slope obtained from the fits corresponding to the cathodic peaks of $NiCo_2S_4/Co_3S_4$ electrode is 0.48, which indicates that the $NiCo_2S_4/Co_3S_4$ electrode materials have more intrinsic diffusional charge-storage properties (Fig. 4e). The charge storage contribution proportions at different scan rates are quantified by the following equation:

$$I(V) = k_1 v + k_2 v^{1/2} \tag{7}$$

where I is the current (A) under a constant voltage (V), $k_1 v$ and $k_2 v^{1/2}$ correspond to the charge contributions of the capacitive and diffusion-controlled processed, respectively. As shown in Fig. S6a (Supporting information), the capacitive contribution of the $NiCo_2S_4/Co_3S_4$ electrode at the scan rate of 5 mV/s is calculated to be 60.1%. Based on the above formula, the values of k_1 (slopes) and k_2 (intercept) can be determined, and several values are given in Fig. S6b (Supporting information).

To further estimate the electrochemical performance of different electrode materials, the electrical impedance spectroscopy (EIS) was carried out as shown in Fig. 4g. The intercept of curves on the X-axis at the high frequency range represents the equivalent series resistance (R_s), which includes the intrinsic resistance of the active materials, bulk resistance of electrolyte, and contact resistance at the interface between electrolyte and electrode. The values of R_s obtained from the $NiCo_2S_4/Co_3S_4$ electrode is 0.77 Ω, lower than that of the NiCo-LDH (0.85 Ω), NCS-2 (0.78 Ω), NCS-6 (0.79 Ω) and NCS-9 (0.84 Ω) electrode. Furthermore, the $NiCo_2S_4/Co_3S_4$ electrode displays the highest line slope at low-frequency region, indicating the excellent behavior of ion diffusion/migration in the electrolyte. The reduced impedance effectively contributes to the fast charge transfer and the diffusion of electrolyte ions in the redox reaction leading to better capacity characteristics. In addition, the $NiCo_2S_4/Co_3S_4$ electrode reveals outstanding long-term cyclic stability with a capacity retention of 89.6% upon 5000 charge/discharge cycles at 10 A/g (Fig. 4h). Moreover, the EIS plots (Fig. S11 in Supporting information) of the electrode taken before and after the cycling tests showed no discernible changes, demonstrating remarkable electrochemical stability.

The excellent specific capacitance, rate performance and cycling stability might be ascribed as follows: Firstly, during the simple two steps of *in-situ* controllable hydrothermal process, functional species of bimetallic active component (Ni and Co) can be incorporated, which is beneficial to provide numerous active sites for the redox reactions and effectively enhance the electrochemical performance. Secondly, the unique hollow porous structure could provide a rapid diffusion of electrolyte with accessible inner/outer surfaces, and accommodate the huge shrinkage and expansion of volume during the process of charge/discharge, guaranteeing the stability of structure and remarkable cycling life. Thirdly, the abundant interfaces of amorphous, low-crystalline, and well crystallized structures, as well as hetero-interfaces can induce strong interfacial electron transfer properties, promote immersion of the electrolyte ions, and provide more interfacial active sites for the redox reaction.

In order to evaluate the practical application of the heterogeneous $NiCo_2S_4/Co_3S_4$ NCs, as shown in Fig. 5a, a hybrid supercapacitor was fabricated using $NiCo_2S_4/Co_3S_4$ as the positive electrode and N-rGO gel as the negative electrode in a 2 mol/L KOH electrolyte (noted as $NiCo_2S_4/Co_3S_4$//N-rGO). The related morphology and characterizations of the N-rGO gel negative electrode are exhibited in Figs. S7-S10. As can be seen from SEM images and N_2 adsorption-desorption isotherms, N-rGO displays a three-dimensional porous structure and a high Brunauer-Emmett-Teller (BET) specific surface area (Figs. S7 and S8). The results of XPS spectra (Fig. S9) verify the N doping of 3D N-rGO. Moreover, the N-rGO electrode demonstrates excellent electric double-layer behavior with a nearly rectangular CV curve from −1.0 V to 0 V, and the shape is hardly changed with the increase of scan rate, as seen in Fig. S10a. Meanwhile, a high specific capacitance (291 F/g) can be arrived at 1 A/g for 3D N-rGO (Fig. S10c).

Comparing the CV profiles of the $NiCo_2S_4/Co_3S_4$ electrode and 3D N-rGO electrode at a scan rate of 5 mV/s (Fig. 5b), the respective operating potential are 0 to 0.6 V and −1.0 V to 0 V, demonstrating that these two electrode materials were suitable for assembling devices with stable and continuous voltage. Fig. 5c presents typical CV curves for $NiCo_2S_4/Co_3S_4$//N-rGO HSC device at various operating potentials, revealing that the working potential can possibly reach up to 1.6 V for the full cell. The CV curves of HSC device at different scan rates between 5 mV/s and 100 mV/s were shown in Fig. 5d. The CV curves combine the distinct faradaic

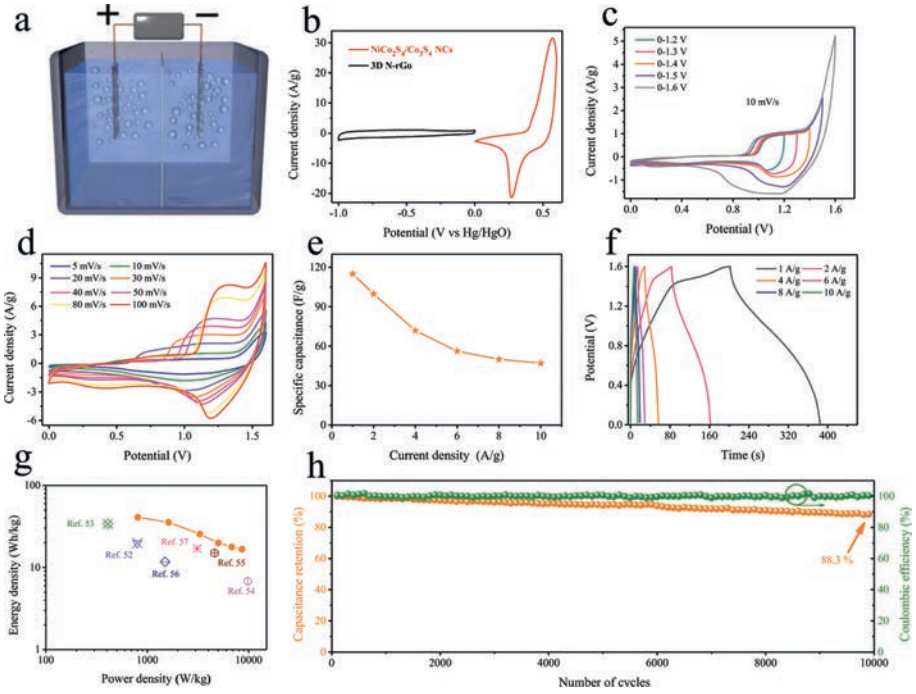

Fig. 5. Electrochemical characterization of the assembled $NiCo_2S_4/Co_3S_4$//N-rGO HSC device: (a) Schematic illustration of the device fabrication. (b) CV curves of the $NiCo_2S_4/Co_3S_4$ and N-rGO electrodes at the scan rate of 5 mV/s. (c) CV curves in different operating voltage windows at a scan rate of 10 mV/s. (d) CV curves at different scan rates. (e) GCD curves at various current densities. (f) The specific capacitances at different current densities. (g) Ragone plots of as-assembled HSC compared to some of the recently reported HSC devices. (h) Cycling life of the device with 10,000 cycles at 10 A/g.

redox behaviors and electric double-layer capacitance. Additionally, along with the increasing of sweep rate, the CV curves slightly change without discernible distortion, suggesting good reversibility and excellent fast charge/discharge performance for the HSC device. This behavior can be attributed to the improved ionic and electronic transport within the electrode materials. As demonstrated in Fig. S12 (Supporting information), the kinetics and internal resistances of the HSC device were also conducted with a frequency range of 100 kHz to 0.01 Hz at a bias potential of 5 mV. From the Nyquist plots, the smaller radius in the high frequency clearly indicates rapid charge kinetics due to the high electrical conductivity and good electrochemical activity of the device.

The GCD analysis (Fig. 5e) collected at different current densities show an asymmetric triangle-like shape with no obvious IR drop, indicating good electrochemical reversibility. Notably, the specific capacitances of the HSC device are calculated to be 115, 99, 71, 56, 50 and 47 F/g, based on the total mass of the active materials at current densities of 1, 2, 4, 6, 8 and 10 A/g, respectively, as shown in Fig. 5f. Fig. 5g exhibits the Ragone plot, which gives the relation between the energy density and power density of the device. The $NiCo_2S_4/Co_3S_4$//N-rGO HSC device obtains a maximum energy density of 40.8 Wh/kg at a power density of 806.3 W/kg and retains 16.7 Wh/kg at 8595.6 W/kg. The achieved value is higher than that of the reported HSCs, such as Ni_3S_2/MWCNT-NC//AC [52], $CoNi_2S_4$//AC [53], $NiCo_2S_4$//AC [54], $NiCo_2S_4$/PRGO//AC [55], Ni_3S_4 (S2)//AC [56], $(Ni_{0.1}Co_{0.9})_9Se_8$@CFC//reduced graphene oxide@CFC (Fig. 5g) [57]. The cycling durability of the HSC is further tested at a current density of 10 A/g up to 10,000 cycles. As shown in Fig. 5h, the device maintains about 88.3% of its initial capacitance after 10,000 cycles, revealing excellent electrochemical stability. Moreover, the HSC device shows nearly 100% Coulombic efficiency throughout the cyclic measurement, further confirming the robust long-term durability. Consequently, the $NiCo_2S_4/Co_3S_4$//N-rGO HSC device with a preeminent electrochemical performance can possess huge potential in energy storage.

In summary, we designed a new strategy of controllable sulfurization to construct a rational design of heterogeneous and low-crystalline architectures that enabled $NiCo_2S_4/Co_3S_4$ nanocages as a battery-type electrode for high-performance HSC. The chemical and macro/microstructural characterizations of the prepared materials revealed the formation of hollow structured $NiCo_2S_4/Co_3S_4$ with abundant hetero-interfaces and comparatively poor crystallinity after controllable hydrothermal methodology from sacrificial template precursors. Combining the tuned crystalline structures and remarkable interfacial electron transfer properties, the resultant $NiCo_2S_4/Co_3S_4$ electrode yielded a high specific capacity of 1023 C/g at a current density of 1 A/g, and an excellent cycling stability of 89.6% after 5000 cycles. Moreover, HSCs assembled with battery-type hollow structured $NiCo_2S_4/Co_3S_4$ NCs as a positive electrode and nitrogen-doped reduced graphene oxide as a negative electrode, exhibited superior energy density of 40.8 Wh/kg and power density up to 8595.6 W/kg, as well as excellent cyclic stability. This rational design offers new opportunities to tailor the inherent crystallinity structure, activate redox-active metal sulfides spices and boost highly-reversible and fast reactions for next-generation energy storage devices.

Declaration of competing interest

The authors declare that they have no known competing financial interests or personal relationships that could have appeared to influence the work reported in this paper.

Acknowledgments

This work was supported by National Natural Science Foundation of China (Nos. 52173255 and 52125202), the Opening Project of the Jiangsu Key Laboratory for Chemistry of Low-Dimensional Materials (No. JSKC20021), PAPD of Jiangsu and the Collaborative

Innovation Center for Advanced Micro/nanomaterials and Equipment (Co-constructed by Jiangsu Province and Ministry of Education).

Supplementary materials

Supplementary material associated with this article can be found, in the online version, at doi:10.1016/j.cclet.2022.01.030.

References

[1] B.Y. Guan, L. Yu, X. Wang, et al., Adv. Mater. 29 (2017) 1605051.
[2] Y. Shao, M.F. El-Kady, J. Sun, et al., Chem. Rev. 118 (2018) 9233–9280.
[3] Q. Ma, Y. Yao, M. Yan, et al., Sci. China Mater. 62 (2019) 1393–1402.
[4] Y. Chen, X. Li, K. Park, et al., J. Am. Chem. Soc. 135 (2013) 16280–16283.
[5] S. Li, J. Fu, G. Miao, et al., Adv. Mater. 33 (2021) 2008424.
[6] Q. Zhang, B. Zhao, J. Wang, et al., Nano Energy 28 (2016) 475–485.
[7] X. Zhao, Y. Wang, Y. Shi, et al., ACS Energy Lett. 6 (2021) 1134–1140.
[8] B. Zhao, D. Chen, X. Xiong, et al., Energy Stor. Mater. 7 (2017) 32–39.
[9] H. Shao, Y.C. Wu, Z. Lin, et al., Chem. Soc. Rev. 49 (2020) 3005–3039.
[10] J. Fu, L. Li, J.M. Yun, et al., Chem. Eng. J. 375 (2019) 121939.
[11] B.Y. Guan, X.Y. Yu, H.B. Wu, X.W.D. Lou, Adv. Mater. 29 (2017) 1703614.
[12] J. Lin, C. Zeng, X. Lin, et al., Adv. Sci. 7 (2020) 2000736.
[13] R. Hou, M. Miao, Q. Wang, et al., Adv. Energy Mater. 10 (2019) 1901892.
[14] Y. Zhang, J. Li, W. Zhao, et al., Adv. Mater. (2021) 2108114.
[15] Y. Bai, C. Liu, Y. Shan, et al., Adv. Energy Mater. (2021) 2100346.
[16] S. Zheng, Y. Sun, H. Xue, et al., Natl. Sci. Rev. 9 (2022) nwab197.
[17] S. Zheng, Y. Ru, H. Xue, H. Pang, Chin. Chem. Lett. 32 (2021) 3817–3820.
[18] Y. Liu, X. Xu, Z. Shao, S.P. Jiang, Energy Stor. Mater. 26 (2020) 1–22.
[19] B.Y. Xia, Y. Yan, N. Li, et al., Nat. Energy 1 (2016) 15006.
[20] T. Wang, Z. Kou, S. Mu, et al., Adv. Funct. Mater. 28 (2018) 1705048.
[21] H. Hu, B. Guan, B. Xia, X.W. Lou, J. Am. Chem. Soc. 137 (2015) 5590–5595.
[22] H. Liu, J. Guan, S. Yang, et al., Adv. Mater. 32 (2020) 2003649.
[23] P. Zhang, B.Y. Guan, L. Yu, X.W.D. Lou, Angew. Chem. Int. Ed. 56 (2017) 7141–7145.
[24] Y. Li, Y. Shan, H. Pang, Chin. Chem. Lett. 31 (2020) 2280–2286.
[25] N. Li, X. Guo, X. Tang, et al., Chin. Chem. Lett. 33 (2022) 462–465.
[26] C. Jing, X. Guo, L. Xia, et al., Chem. Eng. J. 379 (2020) 122305.
[27] Z. Bai, S. Li, J. Fu, et al., Nano Energy 58 (2019) 680–686.
[28] Z. Wang, H. Jia, Y. Cai, et al., Chem. Eng. J. 392 (2020) 123890.
[29] W. Lu, J. Shen, P. Zhang, et al., Angew. Chem. Int. Ed. 58 (2019) 15441–15447.
[30] M. Sun, Z. Li, Q. Fang, et al., J. Mater. Chem. A 8 (2020) 724–734.
[31] X. Yang, J. Mao, H. Niu, et al., Chem. Eng. J. 406 (2021) 126713.
[32] Y. Yan, A. Li, C. Lu, et al., Chem. Eng. J. 396 (2020) 125316.
[33] H. Pang, X. Li, Q. Zhao, et al., Nano Energy 35 (2017) 138–145.
[34] Q. Wang, Y. Luo, R. Hou, et al., Adv. Mater. 31 (2019) 1905744.
[35] L. Kang, M. Zhang, J. Zhang, et al., J. Mater. Chem. A (2020) 25443–25444.
[36] J. Liu, M. Zheng, X. Shi, et al., Adv. Funct. Mater. 26 (2016) 919–930.
[37] H.C. Chen, Y. Qin, H. Cao, et al., Energy Stor. Mater. 17 (2019) 194–203.
[38] C. Huang, X. Song, Y. Qin, et al., J. Mater. Chem. A 6 (2018) 21047–21055.
[39] C. Ren, X. Jia, W. Zhang, et al., Adv. Funct. Mater. 30 (2020) 2004519.
[40] Q. Liu, X. Hong, X. You, et al., Energy Stor. Mater. 24 (2020) 541–549.
[41] F. Xu, N. Chen, Z. Fan, G. Du, Appl. Surf. Sci. 528 (2020) 146920.
[42] S. Sun, T. Zhai, C. Liang, et al., Nano Energy 45 (2018) 390–397.
[43] L. Zhang, L. Dong, M. Li, et al., J. Mater. Chem. A 6 (2018) 1412–1422.
[44] R. Cao, M. Cao, H. You, et al., Natl. Sci. Rev. 7 (2020) 609–619.
[45] X. Yang, P. Deng, D. Liu, et al., J. Mater. Chem. A 8 (2020) 2472–2480.
[46] F. Sun, Q. Li, Y. Bai, et al., Chin. Chem. Lett. 33 (2022) 3249–3254.
[47] X. Wang, F. Huang, F. Rong, et al., J. Mater. Chem. A 7 (2019) 12018–12028.
[48] T.T. Nguyen, D. Mohapatra, D.R. Kumar, et al., Electrochim. Acta 367 (2021) 137226.
[49] B. Jiang, X. Ban, Q. Wang, et al., J. Mater. Chem. A 7 (2019) 24374–24388.
[50] C. Li, J. Balamurugan, N.H. Kim, J.H. Lee, Adv. Energy Mater. 8 (2018) 1702014.
[51] Z. Feng, H. Zou, W. Yang, et al., J. Alloys Compd. 862 (2021) 158586.
[52] C.S. Dai, P.Y. Chien, J.Y. Lin, et al., ACS Appl. Mater. Inter. 5 (2013) 12168–12174.
[53] W. Hu, R. Chen, W. Xie, et al., ACS Appl. Mater. Inter. 6 (2014) 19318–19326.
[54] Y. Zhu, Z. Wu, M. Jing, et al., J. Power Sources 273 (2015) 584–590.
[55] Y. Zheng, X. Wang, W. Zhao, et al., Chem. Eng. J. 333 (2018) 603–612.
[56] H. Wang, M. Liang, D. Duan, et al., Chem. Eng. J. 350 (2018) 523–533.
[57] P. Yang, Z. Wu, Y. Jiang, et al., Adv. Energy Mater. 8 (2018) 1801392.